

STORM IN A “TEACUP”: A RADIO-QUIET QUASAR WITH ≈ 10 KPC RADIO-EMITTING BUBBLES AND EXTREME GAS KINEMATICS

C. M. HARRISON,^{1,*} A. P. THOMSON,¹ D. M. ALEXANDER,¹ F. E. BAUER,^{2,3,4} A. C. EDGE,¹ M. T. HOGAN,¹ J. R. MULLANEY⁵ AND A. M. SWINBANK¹

Draft version November 8, 2021

ABSTRACT

We present multi-frequency (1–8 GHz) VLA data, combined with VIMOS IFU data and *HST* imaging, of a $z = 0.085$ radio-quiet type 2 quasar (with $L_{1.4\text{GHz}} \approx 5 \times 10^{23} \text{ W Hz}^{-1}$ and $L_{\text{AGN}} \approx 2 \times 10^{45} \text{ erg s}^{-1}$). Due to the morphology of its emission-line region, the target (J1430+1339) has been referred to as the Teacup AGN in the literature. We identify “bubbles” of radio emission that are extended ≈ 10 – 12 kpc to both the east and west of the nucleus. The edge of the brighter eastern bubble is co-spatial with an arc of luminous ionized gas. We also show that the Teacup AGN hosts a compact radio structure, located ≈ 0.8 kpc from the core position, at the base of the eastern bubble. This radio structure is co-spatial with an ionized outflow with an observed velocity of $v = -740 \text{ km s}^{-1}$. This is likely to correspond to a jet, or possibly a quasar wind, interacting with the interstellar medium at this position. The large-scale radio bubbles appear to be inflated by the central AGN, which indicates that the AGN can also interact with the gas on $\gtrsim 10$ kpc scales. Our study highlights that even when a quasar is formally “radio-quiet” the radio emission can be extremely effective for observing the effects of AGN feedback.

Subject headings: galaxies: evolution; galaxies: active; galaxies: jets; galaxies: individual (Teacup AGN)

1. INTRODUCTION

There is now general agreement that growing black holes, i.e., active galactic nuclei (AGN) activity, can have a profound impact upon the gas in their host galaxies and beyond. This impact, often termed “AGN feedback”, is a requirement of most models of galaxy formation in order to reproduce the properties of local massive galaxies, the intergalactic medium and intracluster medium (e.g., BH-mass scaling relationships; the galaxy luminosity function; the X-ray temperature-luminosity relationship; e.g., Silk & Rees 1998; Benson et al. 2003; Churazov et al. 2005; Hopkins et al. 2006; Bower et al. 2006; McCarthy et al. 2010; Gaspari et al. 2011; Schaye et al. 2014; Vogelsberger et al. 2014). Observationally, there is convincing evidence that some sort of interaction occurs, although establishing the types of galaxies in which it is important and exactly how the energy couples to the gas is a matter of ongoing research (see reviews in Alexander & Hickox 2012; Fabian 2012; McNamara & Nulsen 2012; Kormendy & Ho 2013; Heckman & Best 2014).

AGN-driven energetic outflows are a promising means by which an AGN can interact with the gas in their larger-scale environment. Observations of AGN, across a wide range of redshifts, have now revealed out-

flows in atomic, molecular and ionized gas that are often identified over kiloparsec scales (e.g., Veilleux et al. 2005; Nesvadba et al. 2006, 2008; Alexander et al. 2010; Feruglio et al. 2010; Lehnert et al. 2011; Greene et al. 2011; Alatalo et al. 2011; Harrison et al. 2012, 2014; Liu et al. 2013; Rupke & Veilleux 2013; Veilleux et al. 2013; Genzel et al. 2014; Arribas et al. 2014; Brusa et al. 2014). A variety of processes have been attributed to driving such outflows, including radio jets, stellar winds, supernovae and quasar disk winds (e.g., Holt et al. 2008; Lehnert et al. 2011; Guillard et al. 2012; Rupke & Veilleux 2013; Zakamska & Greene 2014). Some of the most powerful analyses to address this issue come from combining spatially-resolved, multi-wavelength data sets. In particular, in several AGN with high radio-to-optical luminosity ratios, i.e., “radio-loud” AGN, radio jets appear to be spatially-coincident with outflowing material (e.g., van Breugel et al. 1985; Villar-Martín et al. 1999; Oosterloo et al. 2000; Solórzano-Iñarrea & Tadhunter 2003; Morganti et al. 2005, 2013; Stockton et al. 2007; Nesvadba et al. 2008; Shih et al. 2013; Mahony et al. 2013). However, most AGN are *radio quiet* (e.g., ≈ 85 – 90% for optically-identified quasars; e.g., Kellermann et al. 1989; Zakamska et al. 2004; Lal & Ho 2010) and, crucially, for these sources the driver of the observed outflows remains less clear.

To assess the prevalence, drivers and properties of ionized outflows in low-redshift luminous AGN, we performed multi-component fitting to the emission lines of $\approx 24,000$ $z < 0.4$ optically identified AGN, which are predominantly radio quiet (Mullaney et al. 2013). In this study we found that there is a relationship between the presence of the most extreme ionized gas kinematics and radio luminosity. More specifically, AGN with moderate-

* Email: c.m.harrison@mail.com

¹ Department of Physics, Durham University, South Road, Durham, DH1 3LE, U.K.

² Instituto de Astrofísica, Facultad de Física, Pontificia Universidad Católica de Chile, 306, Santiago 22, Chile

³ Millennium Institute of Astrophysics, Vicuña Mackenna 4860, 7820436 Macul, Santiago, Chile

⁴ Space Science Institute, 4750 Walnut Street, Suite 205, Boulder, CO 80301, USA

⁵ Department of Physics and Astronomy, University of Sheffield, Sheffield, S7 3RH, U.K.

to-high radio luminosities (i.e., $L_{1.4\text{GHz}} \gtrsim 10^{23} \text{ W Hz}^{-1}$) are much more likely to show broad and high-velocity kinematic components in their [O III] $\lambda 5007$ emission-line profiles than AGN with lower radio luminosities.⁷ A similar result was reached by Zakamska & Greene (2014) for 568, $z < 0.8$, type 2 radio-quiet quasars and is also consistent with the results of several other studies with smaller samples of AGN (e.g., Heckman et al. 1981; Wilson & Heckman 1985; Veilleux 1991; Whittle 1992; Nelson & Whittle 1996; Nesvadba et al. 2011; Husemann et al. 2013; Villar Martín et al. 2014). However, there is an ongoing investigation into the origin of the radio emission in radio-quiet AGN and therefore, it is not yet clear what physical processes are responsible for the observed correlation between ionized gas kinematics and radio luminosity (e.g., Mullaney et al. 2013; Zakamska & Greene 2014). Overall, there are three main possibilities: (1) the radio emission is dominated by star formation (e.g., Sopp & Alexander 1991; Condon et al. 2013) and associated stellar winds or supernovae drive the outflows; (2) the presence of compact (i.e., $\lesssim 5 \text{ kpc}$) radio jets/lobes dominate the radio emission (e.g., Kukula et al. 1998; Ulvestad et al. 2005; Singh et al. 2014) and also drive the outflows (e.g., Whittle 1992; Leipski et al. 2006; Mullaney et al. 2013; Kim et al. 2013); (3) the radio emission is dominated by nuclear coronal activity (e.g., Laor & Behar 2008) and/or shocks (Zakamska & Greene 2014; Nims et al. 2014) and quasar winds are responsible for driving the outflows (e.g., Faucher-Giguère & Quataert 2012; Zubovas & King 2012). We now aim to address the outstanding issues of the origin of the radio emission in radio-quiet AGN and which processes drive their observed outflows, by combining high-resolution radio data with spatially-resolved spectroscopy on a well defined sample of optically luminous AGN (Mullaney et al. 2013; Harrison et al. 2014).

In this pilot study, we combine high-resolution radio imaging and spatially-resolved spectroscopy for one radio-quiet type 2 quasar, J1430+1339 (nicknamed the “Teacup AGN”; Keel et al. 2012; see Section 2). This source is drawn from a larger sample of type 2 AGN that host kiloparsec-scale ionized outflows (Harrison et al. 2014). We present new Karl G. Jansky Very Large Array (VLA) continuum observations, new VISIBLE MultiObject Spectrograph (VIMOS) integral field unit (IFU) observations and archival *Hubble Space Telescope* (*HST*) narrow-band and medium-band images. In Section 2 we give background information on this source; in Section 3 we present the details of the data acquisition and reduction; in Section 4 we discuss the observations and their implications; and in Section 5 we give our conclusions. In our analysis we use $H_0 = 71 \text{ km s}^{-1}$, $\Omega_M = 0.27$, $\Omega_\Lambda = 0.73$. Throughout, we relate flux density, S_ν , frequency, ν , and radio spectral index, α , in the form $S_\nu \propto \nu^\alpha$. Images are displayed with north up and east left and positional angles (PAs) are given east of north.

2. J1430+1339: THE “TEACUP” AGN

⁷ The [O III] $\lambda 5007$ emission line traces warm ($T \sim 10^4 \text{ K}$) ionized gas. As a forbidden line, it cannot be produced in the high-density AGN broad-line region and is a good tracer of the low density gas in galaxies over parsecs to tens of kiloparsecs scales (e.g., Wampler et al. 1975; Osterbrock 1989).

This study focuses on the radio-quiet type 2 quasar SDSS J143029.88+133912.0 (J1430+1339) with a redshift of $z = 0.08506$. Using the Sloan Digital Sky Survey (SDSS) spectrum, Reyes et al. (2008) and Mullaney et al. (2013) independently identified this source as a type 2 (“obscured”) AGN. The high [O III] luminosity of $L_{[\text{O III}]} = 5 \times 10^{42} \text{ erg s}^{-1}$ and the bolometric AGN luminosity of $L_{\text{AGN}} = 2 \times 10^{45} \text{ erg s}^{-1}$ (derived from the mid-far-infrared spectral energy distribution [SED]), classifies this source as a type 2 *quasar* (Reyes et al. 2008; Harrison et al. 2014; also see Gagne et al. 2014). The moderate radio luminosity of J1430+1339 ($L_{1.4\text{GHz}} = 5 \times 10^{23} \text{ W Hz}^{-1}$),⁸ results in this type 2 quasar being classified as *radio quiet* in the $\nu L_\nu(1.4\text{GHz})$ - $L_{[\text{O III}]}$ plane (following Xu et al. 1999; Zakamska et al. 2004). Additionally, the far-infrared (FIR; 8–1000 μm) luminosity attributed to star formation is unexceptional, with $L_{\text{IR,SF}} = 3 \times 10^{44} \text{ erg s}^{-1}$, which corresponds to a star formation rate (SFR) of $\approx 7 M_\odot \text{ yr}^{-1}$ using the standard conversion from Kennicutt (1998) but converted to a Chabrier initial mass function (see details in Harrison et al. 2014). Based upon the radio and infra-red luminosities, J1430+1339 appears to be representative of low redshift quasars. However, as noted by Harrison et al. (2014) and Villar Martín et al. (2014), this source lies more than a factor of 10 above the radio-far-infrared correlation (following e.g., Helou et al. 1985; Ivison et al. 2010), making this a *radio excess* source, with a radio excess parameter of $q_{\text{IR}} = 1.3 \pm 0.2$ (Harrison et al. 2014). This implies that processes in addition to star formation are producing the radio emission (such as radio jets, nuclear coronal activity or shocks; see Harrison et al. 2014). In this paper we present new high-resolution radio continuum observations to assess the processes that are producing the radio emission in J1430+1339.

The properties of the ionized gas in J1430+1339 have resulted in recent interest in the source. Using a citizen science campaign to search for candidate AGN-ionized extended emission-line regions (EELRs) in SDSS images, participants of the “Galaxy Zoo” project (Lintott et al. 2008) identified J1430+1339 as having an interesting EELR morphology (Keel et al. 2012; later confirmed by *HST* imaging; Keel et al. 2014). Due to the loop-shaped “handle” of emission-line gas extending $\approx 12 \text{ kpc}$ to the north-east of the SDSS image, Keel et al. (2012) nicknamed this galaxy the “Teacup” AGN (which is the name we will now use). The *HST* imaging also reveals that the Teacup AGN resides in a bulge-dominated galaxy, with shell-like features, indicative of previous merger activity (Keel et al. 2014). The same team recently presented longslit data on the “Teacup” AGN, and used photoionization modelling to demonstrate that the EELR is dominated by photoionization by a central AGN. They suggested that the AGN has dropped in luminosity by one-to-two orders of magnitude over the last $\approx 50,000$ years (Gagne et al. 2014).

Using integral field unit (IFU) spectroscopy we have shown that the Teacup AGN hosts kiloparsec-scale ion-

⁸ The radio luminosity of $L_{1.4\text{GHz}} = 5 \times 10^{23} \text{ W Hz}^{-1}$ is derived using the flux density measurement of $S_{1.4\text{GHz}} = 26.4 \pm 0.4 \text{ mJy}$ in the $\approx 5 \text{ arcsec}$ resolution VLA FIRST imaging by Becker et al. (1995), and assuming a spectral index of $\alpha = -1$.

ized outflows (Harrison et al. 2014). Based upon the catalog of Mullaney et al. (2013) we initially identified a broad [O III] emission-line profile in its SDSS spectrum, indicative of ionized outflows (this was also noted independently by Villar Martín et al. 2014) and then performed observations with Gemini’s Multi-Object Spectrograph (GMOS) IFU, in order to spatially resolve the ionized gas kinematics. These IFU observations revealed a high-velocity kinematic component with $v \approx -800 \text{ km s}^{-1}$, relative to the local gas velocity, located $\approx 1 \text{ kpc}$ from the nucleus. Due to the small field of view of the GMOS IFU used (i.e., $3.5 \times 5 \text{ arcsec}$), the full extent of the emission-line region was not covered by these observations (including the large emission-line loop described above). In this paper we present IFU observations that cover the full $\approx 20 \times 15 \text{ arcsec}$ extent of the EELR, which enables us to trace the full kinematic structure of the ionized gas.

3. DATA ACQUISITION, REDUCTION AND ANALYSIS

For this paper we combine multiple datasets on the Teacup AGN: (1) new radio imaging data obtained with the VLA (Section 3.1); (2) new optical IFU data obtained with ESO-VIMOS (Section 3.2) and (3) archival *HST* imaging (Section 3.3). In this section we give details of the observations, the steps of data reduction and the analyses that we performed on each data set. In Section 4 we discuss the results using the combined data sets.

3.1. VLA data

3.1.1. Observations

We observed the Teacup AGN between December 2013 and May 2014 using the VLA at *L*- and *C*-Band ($\approx 1\text{--}2 \text{ GHz}$ and $\approx 4\text{--}8 \text{ GHz}$ respectively), in both the B- and A-configurations. These observations were taken under ID 13B-127, and were scheduled dynamically to ensure appropriate weather conditions. We bracketed our scans of the Teacup with 2 minute scans of the bright, nearby BL Lac object J1415+1320, which we use for phase referencing. We calibrated both the bandpass and the absolute flux scale using scans of J1331+3030 (3C 286) taken at the beginning and the end of each session. At *L*-Band, we recorded 16 contiguous spectral windows in full polarization of $64 \times 1 \text{ MHz}$ channels each, that yields a total instantaneous bandwidth of 1024 MHz . Accounting for losses due to flagging of radio frequency interference (RFI), the band center is 1.52 GHz . At *C*-Band we recorded data in two frequency bands of eight contiguous spectral windows in full polarization, centered on $\approx 5 \text{ GHz}$ and $\approx 7 \text{ GHz}$, with each spectral window consisting of $64 \times 2 \text{ MHz}$ channels, yielding $1024 \times 2 \text{ MHz}$ channels in total. The raw visibilities of the VLA data were calibrated locally using Version 1.2.0 of the CASA VLA Calibration pipeline.⁹

3.1.2. Radio maps and analysis

Below we describe a number of maps that we created from our data at different resolutions and with different frequency centroids. The details of the synthesized beams and the noise in each map are summarized in Table 1. We also provide details of how we calculated flux

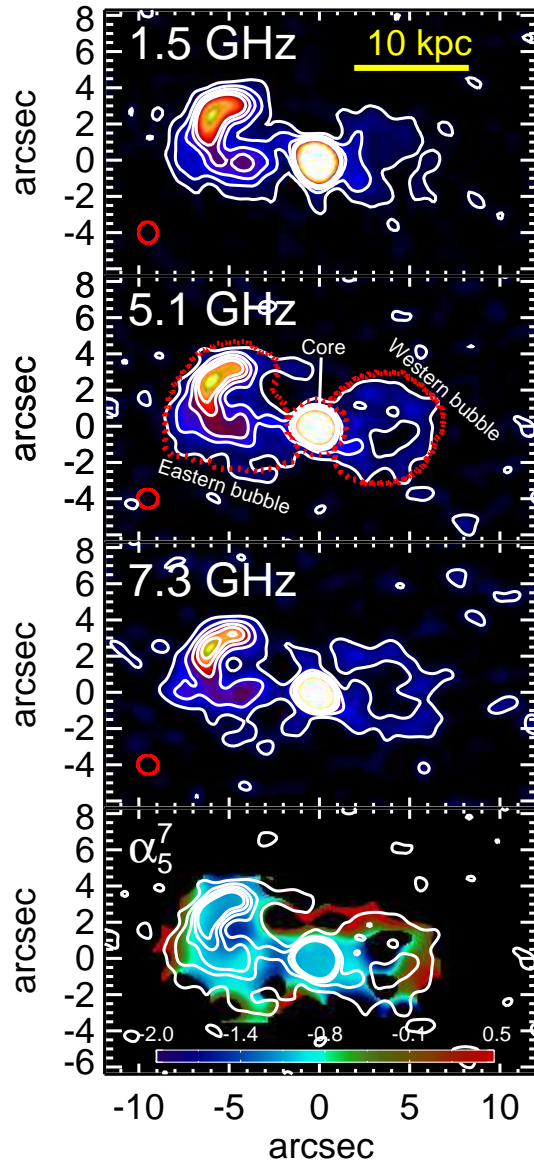


FIG. 1.— Our VLA data for the Teacup AGN at three different observed-frame frequencies (from top-down: 1.52 GHz; 5.12 GHz; 7.26 GHz), which have been matched to the same spatial resolution (see Section 3.1.2). The bottom panel shows a spectral index map using the full *C*-band data (α_5^7), where values are only shown for pixels with an uncertainty ≤ 0.25 . The overlaid contours in this bottom panel are from the 5.12 GHz map. The contours in each panel indicate levels of $[2, 6, 10, 14, 18]\sigma$. The red ellipses represent the beams for each map and the yellow bar in the top panel represents 10 kpc in length. We observe three distinct spatial structures: a $\approx 12 \text{ kpc}$ eastern bubble, a $\approx 11 \text{ kpc}$ western bubble and a bright core. The red dotted contours overlaid on the 5.12 GHz image define the regions that we used for calculating the flux densities and sizes of these structures. The regions of bright emission show steep spectral indices of $\alpha_5^7 \approx -1$. The SED for each of these structure is shown in Figure 2.

densities, their uncertainties and spectral indices for the radio structures that we identified. These values are summarized in Table 2.

In the top panel of Figure 1 we show the *L*-Band, A-configuration VLA data (band center is 1.52 GHz), mapped with a ROBUST=0.5 weighting scheme and no additional tapering in the *uv* plane. We achieve a synthesized beam of $\approx 1 \text{ arcsec}$. In the second and third panels of Figure 1, we show maps from two sub-sets of the *C*-

⁹ <https://science.nrao.edu/facilities/vla/data-processing/>

TABLE 1
PROPERTIES OF RADIO IMAGES

Obs. Frequency (GHz)	Beam HPBW (arcsec)	Beam PA (degrees)	Noise (μ Jy)	Figure
1.52	1.17×1.04	-172	38	1
5.12	1.13×1.04	80	16	1
7.26	1.14×1.03	74	15	1
6.22	0.51×0.38	-61	10	3
6.22	0.37×0.24	-88	18	3(a)
5.12	0.50×0.30	87	28	4
7.26	0.36×0.21	86	27	4

NOTE. — A summary of the central observed frequencies, synthesized beams and noise of the main radio maps used in this work. In Section 3.1.2 we describe which sub-sets of the VLA data went into each map and how they were produced. The final column gives the figure numbers where the maps are shown.

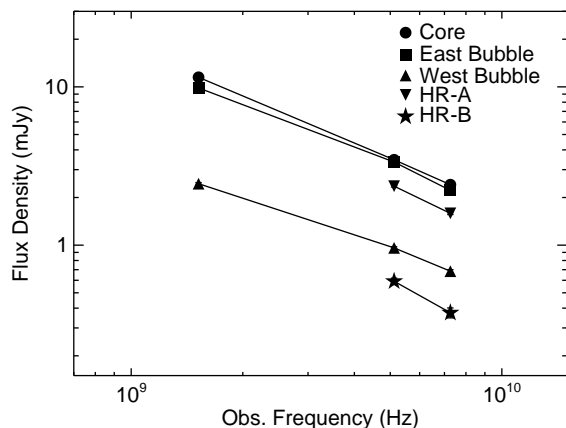


FIG. 2.— The VLA data for each of the spatial structures identified in Figure 1 and Figure 3. We show a SED for each of these structures, where we have fit a piecewise power-law between each data point. The error bars are plotted but are generally smaller than the symbol sizes. These data are tabulated in Table 2. While all of the features are dominated by steep spectral indices (i.e., $\alpha \approx -1$) we note that there is some variation within individual regions (see Figure. 1).

band data, centered at 5.12 GHz and 7.26 GHz that are mapped by weighting the uv data with Gaussian tapers of FWHM=120 k λ and 100 k λ , respectively, to achieve a close approximation with the resolution of the L -band imaging (see Table 1). In the bottom panel of Figure 1 we show a radio spectral index map (between 7 GHz and 5 GHz; α_5^7) from the full C -band spectral data set that was mapped using the multi-scale, multi-frequency synthesis (MSMFS) imaging mode in CASA. The resolution of this spectral index map is 2.05×1.78 arcsec (PA = 74°).

From the three matched-resolution maps described above (Figure 1), we identify three spatial structures: a bright eastern bubble, a fainter western bubble, and a bright core. We measured the flux densities at 1.52 GHz, 5.12 GHz and 7.26 GHz of these features, from the maps shown in Figure 1, by integrating in polygons around each feature (with the edges of the polygons motivated by the 2σ contours in the 5.12 GHz map; see Figure 1). The measured flux densities are reported in Table 2, where the uncertainties correspond to the noise in the respective maps. Using our three-band radio photometry we fit piecewise power-law SEDs between 1.52–5.12 GHz and

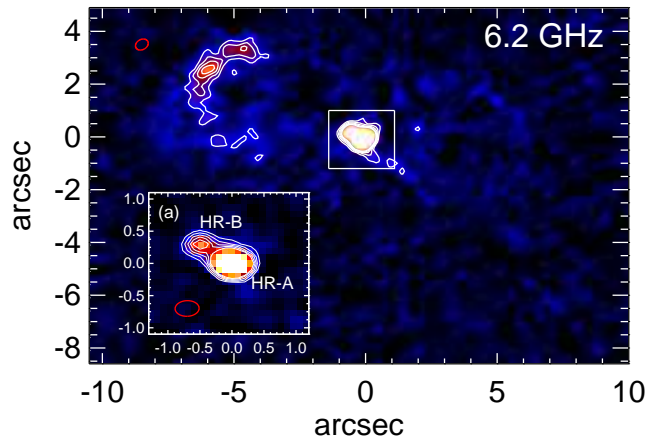


FIG. 3.— Our high-resolution VLA data for the Teacup AGN at observed-frame 6.22 GHz. The eastern bubble and bright core can clearly be observed, whilst some of the fainter extended emission has been resolved out (see Figure 1). Inset (a) shows our highest resolution map (see Table 1), zoomed-in around the white box indicated in the main panel. The contours in both maps are at levels of $[5, 8, 11, \dots]\sigma$. The red ellipses represent the beams. These data clearly show that the bright core, observed in Figure 1, is composed of two spatial structures: a bright central structure (HR-A) and a fainter structure (HR-B) ≈ 0.8 kpc to the north east (PA $\approx 60^\circ$). The HR-B structure is very closely aligned in PA with the brightest region on the edge of the eastern bubble.

between 5.12–7.26 GHz (Figure 2) and calculate the spectral indices ($\alpha_{1.5}^5$ and α_5^7 ; Table 2). To reflect the variation of the spectral indices within each region, in Table 2, we also quote the 1σ scatter, within these regions, derived from the spectral index map shown in Figure 1. We note that the total 1.52 GHz flux density across all regions, seen in this ≈ 1 arcsec resolution L -band map, is $S_{1.5 \text{ GHz}} = 23.79 \pm 0.07$ mJy; however, by re-imaging our L -band data to a resolution 4.59×4.18 arcsec we recovered a total of $S_{1.5 \text{ GHz}} = 25.9 \pm 0.1$ mJy. We thus conclude that ≈ 2 mJy of the L -band radio flux in the Teacup AGN is produced in a diffuse, low surface brightness halo surrounding the core and bubbles, whose emission is resolved-out in our higher-resolution continuum maps.

To search for spatial structures on scales smaller than ≈ 1 arcsec, we make use of the C -band data at full resolution. In Figure 3 we show a ROBUST=0.5 weighted map, created from the B- and A-configuration, across the entire C -band, centered at 6.22 GHz. In this ≈ 0.5 arcsec resolution map the fainter western bubble is resolved out, while the core appears to be slightly elongated along a position angle of PA $\approx 60^\circ$; i.e., in line with the position angle connecting the core to the brightest region in the eastern bubble (see Table 2). Inset (a) of Figure 3 shows our highest, ≈ 0.3 arcsec, resolution C -band map of the core, comprising only of the A-configuration uv data that is mapped with super-uniform weighting in CASA. In this map, the core is clearly resolved into two structures, which we label “High Resolution” (HR)-A and HR-B. HR-B, with peak position: $14^{\text{h}}30^{\text{m}}29^{\text{s}}.902$, $+13^\circ39'12''.15$, is located 0.5 arcsec (≈ 0.8 kpc) to the north-east, at PA $\approx 60^\circ$, of HR-A which has peak position: $14^{\text{h}}30^{\text{m}}29^{\text{s}}.873$, $+13^\circ39'11''.90$. To measure the 5 GHz and 7 GHz flux densities of these two structures we fit super-uniform weighted 5 GHz and 7 GHz maps with two beams (i.e., two unresolved components; Figure 4). The majority of the flux in the core is indeed

TABLE 2
RADIO PROPERTIES OF SELECTED STRUCTURES

Structure	D (1)	PA (2)	$S_{1.5\text{ GHz}}$ (3)	$S_{5\text{ GHz}}$ (4)	$S_{7\text{ GHz}}$ (5)	$\alpha_{1.5}^5$ (6)	α_5^7 (7)	Variation in α (8)
Matched Resolution (Figure 1)								
Core	1.5[2]	0	11.49[4]	3.462[16]	2.410[15]	-0.988[5]	-1.04[2]	± 0.08
Eastern bubble	7.9[5]	66	9.85[4]	3.350[16]	2.219[15]	-0.888[5]	-1.18[2]	± 0.3
Western bubble	6.9[5]	-90	2.45[4]	0.961[16]	0.685[15]	-0.77[2]	-0.98[8]	± 0.6
High Resolution (Figure 3 and Figure 4)								
HR-A	$\lesssim 0.4$	-	-	2.36[3]	1.59[3]	-	-1.13[6]	-
HR-B	$\lesssim 0.4$	-	-	0.59[3]	0.37[3]	-	-1.3[2]	-

NOTE. — The sizes, flux densities and spectral indices of the structures identified in the VLA data of the Teacup AGN (see Figure 1 and Figure 3). (1) The projected size of each structure (in arc seconds) based on the 5 GHz images, measured by taking a vector from the central core peak to the edge of each region (in the case of HR-A and HR-B we quote the HPBW); (2) The PA (in degrees) of the axis that the distances, D , were measured (for the eastern bubble this is in the direction to the brightest knot); (3)–(5) The observed-frame flux densities in mJy; (6) & (7) The spectral indices calculated from the quoted flux densities; (8) The scatter of the α values within the defined regions (see Figure 1). In each column the number in square brackets gives the uncertainty on the last decimal place. We estimate an additional $\approx 5\%$ ($\approx 15\%$) uncertainty on the flux densities of the core and eastern bubble (western bubble) due to the uncertain definitions of the chosen regions (Figure 1).

inside two unresolved structures (corresponding to HR-A and HR-B) at both 5 GHz and 7 GHz. Therefore, these structures are unresolved at a half-power beam width of $\text{HPBW} \approx 0.4$ arcsec (i.e., ≈ 0.6 kpc), which can be taken as very conservative upper limits on their intrinsic sizes. Figure 4 reveals low surface brightness emission (at $\approx 3\sigma$) between the structures in the residual image. Furthermore, the combined 5 GHz flux density of HR-A and HR-B ($S_{5\text{ GHz}} = 2.95$ mJy; Table 2) is less than that of the total core structure from the lower resolution map ($S_{5\text{ GHz}} = 3.46$ mJy), implying a further ≈ 0.5 mJy of diffuse material that may exist inside the core that is not part of these two dominant structures.

3.2. VIMOS IFU data

3.2.1. VIMOS IFU data: observations

We observed the Teacup AGN with the VIMOS (Le Fèvre et al. 2003) instrument installed on the ESO/VLT telescope between 2014 March 9 and 2014 March 10 (Program ID: 092.B-0062). The seeing was < 0.9 arcsec throughout. The observations were carried out in IFU mode using the 0.67 arcsec fibre, which provides a field-of-view of 27×27 arcsec, and the HR-Orange grism, which provides a wavelength range of $5250\text{Å} - 7400\text{Å}$ at a spectral resolution of ≈ 2650 . By using the widths of sky-lines from our observations we found that observed resolution was $\text{FWHM} = 105 \pm 8 \text{ km s}^{-1}$ around $\lambda \approx 5400 \text{Å}$ (i.e., around the observed wavelength of $[\text{O III}]\lambda 5007$). We corrected our measurements for this instrumental resolution. During the observations the target was dithered around the four quadrants of the VIMOS IFU. There were nine on-source exposures performed, each of 540 seconds, resulting in a total on-source exposure time of 4860s. The on-source exposures were interspersed with three on-sky exposures, that were used for sky-subtraction. Flat field frames and arc-lamp frames were observed periodically during the observations. A standard star, taken under similar conditions to the science observations was also observed.

The data reduction on the VIMOS data was performed using the standard ESOREX pipeline, which includes bias subtraction, flat-fielding and wavelength calibration. The standard star was reduced in an identi-

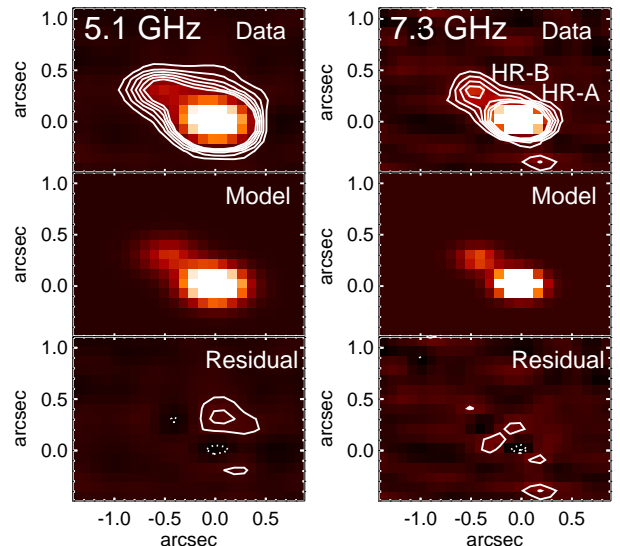


FIG. 4.— Our highest resolution (≈ 0.4 arcsec; see Table 1) VLA data at 5.12 GHz and 7.26 GHz for the central few arc seconds of the Teacup AGN. We have labeled the two unresolved structures HR-A and HR-B, which we identified in Figure 3. The top row shows the data, the second row shows our fits of two beams to these data (“model”) and the bottom row shows the data minus the fit (“residual”; see Section 3.1.2). In each panel the contours represent levels of $[\dots, -7, -5, -3, 3, 5, 7, \dots]\sigma$, where the negative contours are dotted lines and positive contours are solid lines. The majority of the flux is inside two unresolved beams (corresponding to HR-A and HR-B) with some low-significance emission between these two structures. The flux densities and spectral indices (α_5^7) for these two structures are provided in Table 2.

cal manner to the science frames and ESOREX was used to apply the flux calibration. Data cubes were constructed from the individually sky-subtracted, reduced science frames and consequently the final data cube was created by median combining these cubes using a three-sigma clipping threshold.

3.2.2. VIMOS IFU data: emission-line fitting

Our IFU data for the Teacup AGN covers $\approx 40 \times 40$ kpc, which means that we can trace the kinematic structure over the full extent of the EELR. The analysis performed on the IFU data in this work closely follows the methods described in detail in Section 3 of Harrison et al. (2014);

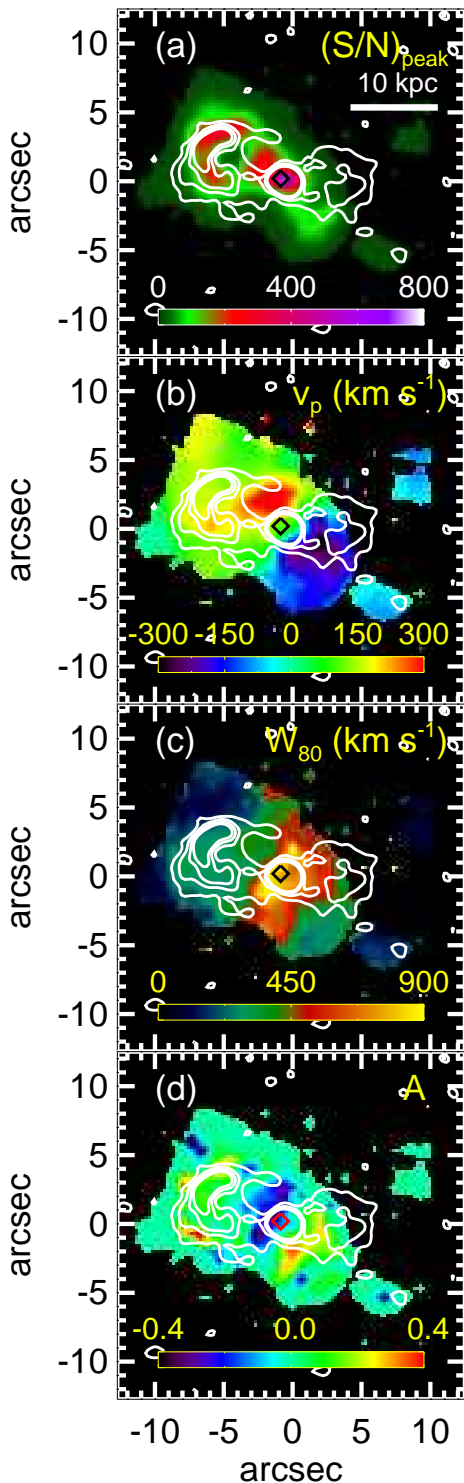


FIG. 5.— Our VIMOS IFU data for the Teacup AGN. These maps characterize the [O III] emission-line profiles, at each spatial pixel, using the non-parametric definitions described in Section 3.2. From top-to-bottom: (a) The signal-to-noise of the peak flux density; (b) the velocity of the peak flux density; (c) the emission-line width; (d) the asymmetry of the emission-line profile. The contours in each panel show the 5 GHz radio data from Figure 1. The diamond in each panel shows the position of the HR-B radio structure seen in Figure 3. The dominant velocity gradient seen in panel (b) appears to be independent of the distribution of radio emission; however, there is bright ionized gas associated with the luminous eastern radio bubble seen in panel (a). Panels (c) and (d) reveal very broad and asymmetric emission-line profiles around the position of the HR-B radio structure, this is due to an additional high-velocity kinematic component at this location (see Figure 6).

therefore, we only give brief details here.

To account for the complexity in the emission-line profiles we opted to use non-parametric definitions to characterize the emission-line profiles within each pixel of the IFU data. In this work we use the following definitions:

1. The peak signal-to-noise, $(S/N)_{\text{peak}}$, which is the signal-to-noise of the emission-line profile at the peak flux density. This allows us to identify the spatial distribution of the emission-line gas, including low surface-brightness features.
2. The “peak velocity” (v_p), which is the velocity of the emission-line profile at the peak flux density. For the Teacup AGN, this traces the velocity structure of the dominant narrow component of the emission-line profile (see Harrison et al. 2014).
3. The line width, W_{80} , which is the velocity that contains 80% of the emission-line flux. This is equivalent to $1.088 \times \text{FWHM}$ for a single Gaussian profile.
4. The asymmetry value (A ; see Liu et al. 2013), which is defined as

$$A \equiv \frac{(v_{90} - v_{50}) - (v_{50} - v_{10})}{W_{80}}, \quad (1)$$

where v_{10} , v_{50} , v_{90} , are the velocities of at 10th, 50th and 90th percent of the cumulative flux, respectively. A very negative value of A means that the emission-line profile has a strong blue wing, while $A = 0$ indicates that it is symmetric.

To illustrate the kinematic structure of the ionized gas, using our IFU data, we use the [O III] $\lambda 5007$ emission line as it is the brightest line in the spectra and it is not blended with other emission lines. In Figure 5 we show four maps, produced using this [O III] emission line, corresponding to the four non-parametric values described above. The values were calculated at each pixel of the data cube following the methods of Harrison et al. (2014). Briefly, we first fit the emission-line profiles (weighting against wavelengths with bad sky lines) with multiple Gaussian components before using the emission-line fits to define each of these four values. By using the emission-line fits we are able to define our non-parametric values even in regions of low signal-to-noise (see Harrison et al. 2014). Values are assigned only to pixels where the emission-line was detected with $(S/N)_{\text{peak}} \geq 5$. In Figure 5, we re-sampled the pixel scale of the maps up by a factor of three, solely for the purposes of a clearer comparison to the morphology of the radio data.

We extracted spectra from different spatial regions of the IFU data cube, where the regions were motivated by the morphology of the radio emission. These spectra were obtained by summing the spectra from the pixels in the vicinity of the three regions shown in Figure 6: (1) the eastern edge of the eastern bubble; (2) the western edge of the western bubble; and (3) the region around the HR-B radio structure. We fit the [O III] emission-line profiles of these spectra in an identical manner to that outlined above for the individual spatial pixels. The fits to the spectra are shown in Figure 6, and the non-parametric values, derived from these fits are given in Table 3. We calculated uncertainties by fitting to 10^4 mock

TABLE 3
[O III] EMISSION-LINE PROFILE PROPERTIES FROM SELECTED
REGIONS

Region	(S/N) _{peak}	v_p (km s ⁻¹)	W_{80} (km s ⁻¹)	A
HR-B region	640	147 ⁺¹¹ ₋₄₀	920 ⁺⁵⁰ ₋₁₂₀	-0.19 ^{+0.04} _{-0.15}
East bubble edge	805	150 ⁺⁷⁰ ₋₄₀	290 ⁺²⁰ ₋₅₀	0.14 ^{+0.02} _{-0.15}
West bubble edge	5	-110±20	320±70	0(*)

NOTE. — The peak signal-to-noise (S/N)_{peak}, peak velocity (v_p), line-width (W_{80}) and asymmetry (A) values for the [O III] emission-line profiles extracted from labelled regions in Figure 6. The upper and lower limits on the values of HR-B and the eastern bubble, reflect the full range in values of the individual pixels inside the defined regions. As the western bubble is not detected in individual pixels (Figure 5), we provide the 2σ uncertainties on the values for this region (see Section 3.2).

* As only one Gaussian component is fit to the emission-line profile of the western bubble, $A = 0$ by default (see Section 3.2).

spectra that were created by taking the best fit model and adding random Gaussian noise. We found that these formal uncertainties were very small (i.e., $\lesssim 10\%$) for the fits to emission-line profiles of the eastern bubble region and HR-B region and do not reflect the true uncertainties, which are dominated by the range in values within each region. Therefore, in Table 3 we provide the range of each value across the individual pixels within the regions.

3.3. HST imaging

The Teacup AGN has been observed with *HST* and the data is published in Keel et al. (2014). We show the *HST* data in this work to compare the emission-line and continuum morphologies to our radio data and IFU data (see Figure 6). Narrow-band images around the [O III] $\lambda 5007$ and H α + [N II] emission lines were taken using the FR551N and FR716N filters, respectively, on the Advance Camera for Surveys (ACS) instrument. The continuum emission, in the wavelength region of these two emission lines, was observed using the medium-band filters F621M and F763M on the Wide-Field Camera 3 (WFC3) instrument (the details of all of these *HST* observations can be found in Keel et al. 2014). We applied a small astrometric correction to register the astrometry of the *HST* images with the SDSS position of the Teacup AGN and our IFU data. In the left column of Figure 6 we show the continuum-free emission-line images around [O III] $\lambda 5007$ and H α + [N II] and the average of the two line-free continuum images, all on a logarithmic scale. In the main panel of Figure 6 we also show a three-color composite image where red and blue are the two continuum images (resulting in a purple continuum color) and green is the [O III] narrow-band image. Subtle features of dust lanes can be seen in the *HST* continuum images, north-west of the core (see Keel et al. 2014). To illustrate where these dusty regions are, in the inset of Figure 6, we created a pseudo-extinction map where we have divided the two continuum images. This map clearly shows a variation of optical colors in the dustier regions identified by Keel et al. (2014), which is also confirmed by the spatial variation of the H α /H β emission-line ratio observed by Gagne et al. (2014).

4. RESULTS AND DISCUSSION

In the previous section we presented a variety of data on the Teacup AGN, a $z = 0.085$ type 2 radio-quiet quasar (see Section 2 for background information), these were: high-resolution radio imaging at 1–8 GHz (Figure 1 to Figure 4); optical IFU data (Figure 5) and *HST* emission-line and continuum images (Figure 6). Our combined data sets have revealed a number of interesting kinematic and morphological structures in the Teacup AGN and we have summarized the most interesting features in a schematic diagram in Figure 7. In this pilot study, for future work on larger samples of radio-quiet AGN, the aim is to understand the relationship between the ionized gas kinematics and the radio emission from this source. In the following sub-sections we describe our main results and discuss some possible interpretations of the observations.

4.1. Summary of the source structure

Our VLA radio imaging of the Teacup AGN reveals two steep spectrum ($\alpha_5^7 \approx -1$; see Table 2) radio structures, extending ≈ 10 – 12 kpc each side of a central steep spectrum core (see Figure 1). These structures appear to be bubbles filled with low surface brightness extended emission that have brighter edges. There is a flattening of the spectral indices towards the edges of the bubbles, which is most noticeable in the western bubble, where $\alpha_5^7 \gtrsim -0.8$. Overall the total 1.5 GHz radio emission is divided such that $\approx 47\%$ of the emission is found in the two radio bubbles, $\approx 44\%$ in a core region and $\approx 9\%$ is likely to be in an extended diffuse structure (see Section 3.1.2 and Table 2). The brighter eastern bubble is most luminous on the eastern edge, where it is spatially co-incident with an arc of luminous ionized gas emission, seen in both [O III] and H α (see Figure 5 and Figure 6). The *HST* imaging also reveals that this gas has a filamentary structure that broadly follows the curvature of the radio bubble (Figure 6). The [O III] and H α emission is much fainter at the location of the western radio bubble (Figure 6). The gas may be misaligned with the ionizing radiation at this point or, alternatively, a low gas density could explain both the low radio luminosity and lack of bright ionized gas emission at this position.

The *kinematic* structure of the ionized gas does not obviously trace the morphology of the radio bubbles (see Figure 5). The largest velocity gradient (with $v_p \approx \pm 300$ km s⁻¹) is found within the host galaxy, extending to ≈ 5 kpc each side of the core with PA $\approx 45^\circ$, i.e., mis-aligned with the radio bubbles by $\approx 20^\circ$. If this gas is a rotational kinematic component, due to the host galaxy’s gravitational potential, it implies a dynamical galaxy mass of $\approx 10^{11} M_\odot$. The gas at the edge of the eastern bubble has a velocity offset of $v_p = 150$ km s⁻¹ relative to the systemic, or ≈ -150 km s⁻¹ relative to the possible ≈ 300 km s⁻¹ “rotational” component near this position. The gas at the edge of the western bubble has a velocity of $v_p = -110$ km s⁻¹ or ≈ 190 km s⁻¹ relative to the ≈ -300 km s⁻¹ “rotational” component. Therefore, the gas in the regions around and beyond the radio bubbles may be decoupled from the possible “rotational” kinematic component. The emission-line profiles on the edges of both bubbles have a moderate emission-line width of $W_{80} \approx 300$ km s⁻¹, compared to those in

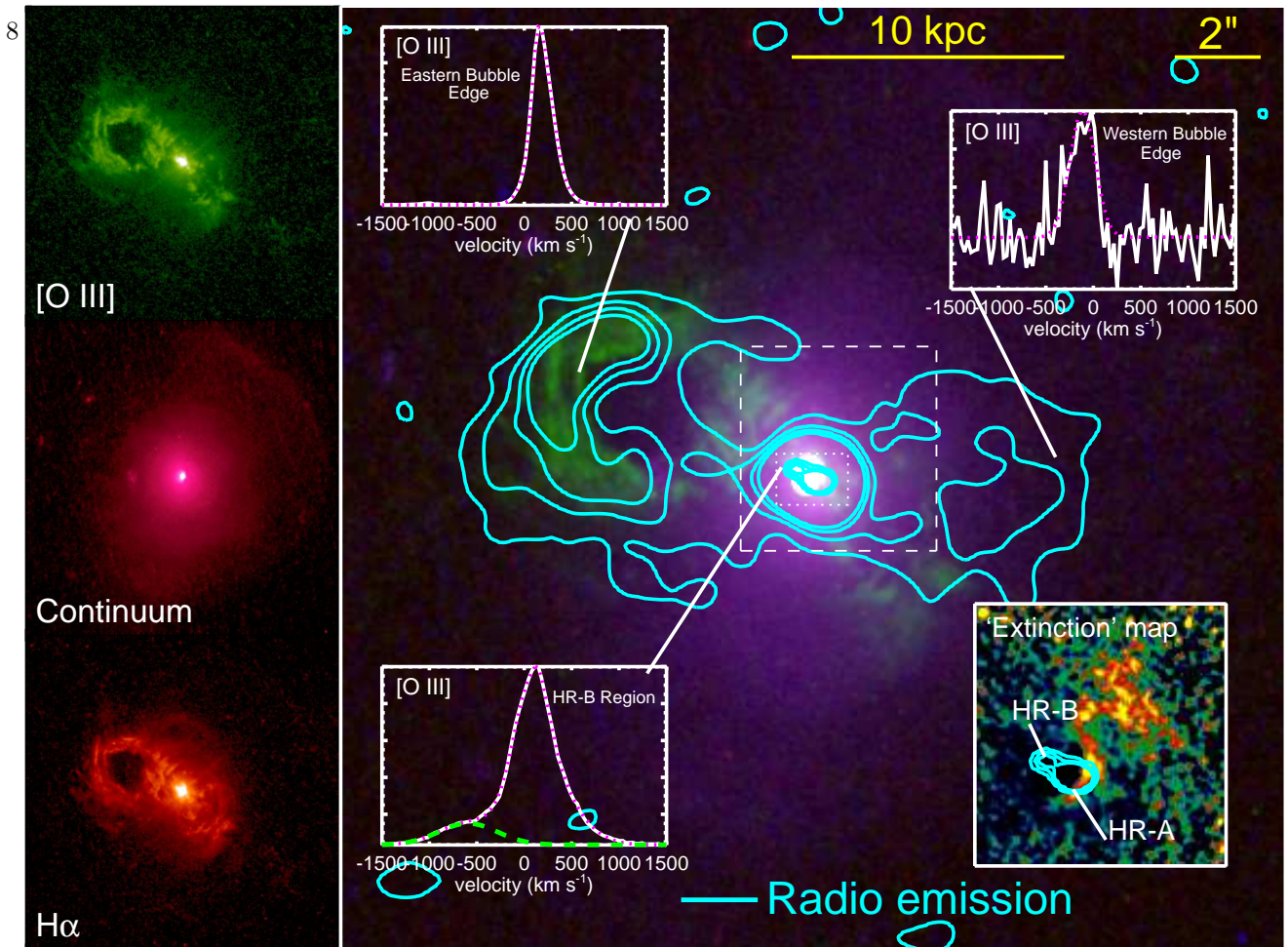


FIG. 6.— *HST* images for the Teacup AGN (described in Section 3.3). *Top Left*: Narrow-band image centered on $[\text{O III}]\lambda 5007$. *Middle Left*: Line-free continuum image. *Bottom Left*: Narrow-band image centered on $\text{H}\alpha$. *Right*: Composite image of the continuum image (shown in purple) and $[\text{O III}]\lambda 5007$ emission (shown in green). The contours represent the 5.2 GHz radio emission from Figure 1, except within the dotted white box where the contours represent the high-resolution 6.2 GHz data from Figure 3. The three inset $[\text{O III}]\lambda 5007$ emission-line profiles are from our VIMOS IFU data cubes, extracted from the specified regions (see Section 3.2). The fits to the spectra are overlaid as magenta dotted lines and the values derived from these fits are shown in Table 3. The highest-velocity kinematic component ($v = -740 \text{ km s}^{-1}$; see Section 4.1) is overlaid as a dashed green line on the “HR-B Region” emission-line profile. The inset on the bottom-right is a pseudo-extinction map, extracted from the region indicated by the dashed white box (see Section 3.3). Overlaid as contours are the high-resolution 6.2 GHz radio data (see Figure 3). In this inset, the dusty regions can be observed, as brighter regions, extending from the core to ≈ 2 arcsec north west of the nucleus. The radio structures are preferentially orientated away from the most dusty region.

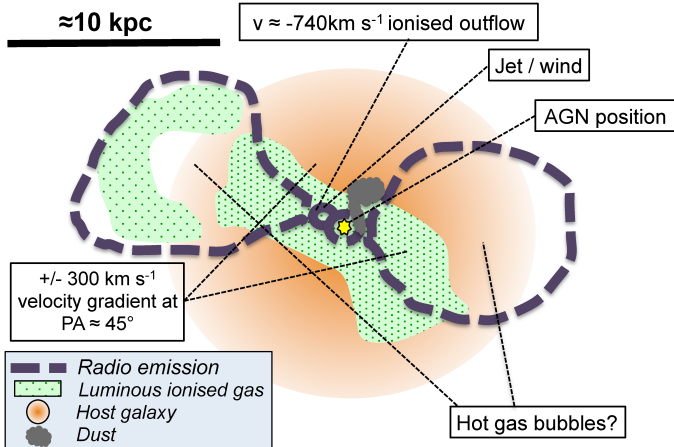


FIG. 7.— A schematic diagram of the Teacup AGN to summarize the results of the data presented in this paper (see Section 4.1). We have highlighted the region of luminous ionized gas with dotted-green shading; however, we note that low surface brightness ionized gas is found over a much larger region (Figure 5).

the central few kiloparsecs which are typically $\approx 500\text{--}900 \text{ km s}^{-1}$ (see Figure 5). We discuss the possible origin

of the $\approx 10\text{--}12 \text{ kpc}$ radio bubbles and associated arc of ionized gas in Section 4.3.

Our highest resolution radio image of the Teacup AGN (Figure 3) reveals that the bright central core, identified in Figure 1, is dominated by two unresolved structures (the resolution is $\text{HPBW} \approx 0.6 \text{ kpc}$); a bright central structure (PA $\approx 60^\circ$) and a fainter structure $\approx 0.8 \text{ kpc}$ to the north east (PA $\approx 60^\circ$). We named these structures “HR-A” and “HR-B”, respectively. Two intriguing points should be noted about the “HR-B” structure: (1) it is approximately along the same axis as the large eastern bubble (with respect to the central core) and (2) it is co-located with a high-velocity (blue-shifted) ionized gas component (see Figure 6). We note that this high-velocity kinematic component has also been observed with GMOS-IFU observations of this source (Harrison et al. 2014 and W. Keel priv. comm.). This high-velocity kinematic component results in the highest observed line widths of $W_{80} \approx 900 \text{ km s}^{-1}$ and the most negative asymmetry values (i.e., $A \lesssim -0.2$) observed in the Teacup AGN (Figure 5). This kinematic component has a velocity $v = -590 \text{ km s}^{-1}$ with respect to the systemic, or

$v = -740 \text{ km s}^{-1}$ with respect to the local velocity (i.e., with respect to v_p ; see Figure 6) and has a line width of $\text{FWHM} = 720 \text{ km s}^{-1}$. These values correspond to a maximum velocity of $v_{\text{max}} \approx 1100 \text{ km s}^{-1}$, using the commonly used definition of $v_{\text{max}} = |v| + \frac{1}{2}\text{FWHM}$ (e.g., Rupke et al. 2005a,b). Both HR-A and HR-B have steep radio spectra, with $\alpha_7^5 = -1.13 \pm 0.06$ and -1.3 ± 0.2 , respectively (see Table 2). In the following sub section we explore the possible origins of these two structures and their connection to the ionized gas kinematics.

4.2. What powers the core radio emission and outflow?

In this subsection we discuss which processes may be producing the radio emission in the core of the Teacup AGN (see Figure 3 and Figure 4) and what is responsible for driving the high-velocity ionized outflow associated with the “HR-B” radio structure (see Figure 5 and Figure 6).

4.2.1. Star formation

Star formation is a possible candidate to produce both the radio emission in the core and also drive outflows via stellar winds and supernovae. The radio luminosity in the core of the Teacup AGN is $L_{1.4\text{GHz}} = 2 \times 10^{23} \text{ W Hz}^{-1}$, which is close to the proposed luminosity boundary between star-formation dominated and AGN-dominated radio emission in low redshift quasars (i.e., $L_{1.4\text{GHz}} \approx 3 \times 10^{23} \text{ W Hz}^{-1}$ for $0.2 < z < 0.3$; Kimball et al. 2011; Condon et al. 2013). The Teacup AGN has a FIR luminosity due to star formation of $L_{\text{IR,SF}} = 3 \times 10^{44} \text{ erg s}^{-1}$ (Harrison et al. 2014). Assuming that the majority of this FIR emission is found in the central few kiloparsecs, the radio flux in the core region is a factor of ≈ 6 above the radio-FIR correlation of star-forming galaxies (e.g., Helou et al. 1985; Bell 2003; Ivison et al. 2010), which would indicate that star formation does not dominate the radio emission in the core.

Another possibility to explore is whether or not the HR-B radio structure (Figure 3) is associated with a compact star-forming region that is responsible for driving the high-velocity gas we see co-located with this structure (with $v = -740 \text{ km s}^{-1}$ and $v_{\text{max}} \approx 1100 \text{ km s}^{-1}$; Figure 6). Indeed, extremely compact star forming regions, with SFRs of $\approx 200 \text{ M}_{\odot} \text{ yr}^{-1}$ and sizes $\approx 100 \text{ pc}$, have been attributed to driving $\approx 1000 \text{ km s}^{-1}$ outflows (Heckman et al. 2011; Diamond-Stanic et al. 2012; Sell et al. 2014). However, maximum velocities as high as that observed around the HR-B radio structure (i.e., $v_{\text{max}} \approx 1100 \text{ km s}^{-1}$) are not seen in non-AGN host galaxies with SFRs comparable to that of the Teacup AGN (i.e., SFRs $\approx 10 \text{ M}_{\odot} \text{ yr}^{-1}$; e.g., Genzel et al. 2011; Arribas et al. 2014) and compact starbursts are often associated with flatter radio spectral indices than that observed here (Murphy et al. 2013). We further disfavor the star formation scenario because: (1) there are not two continuum peaks observed in the *HST* imaging (i.e., to correspond to both the HR-A and HR-B radio structures); (2) HR-B is unlikely to be an obscured star-forming region because the dust in this source is not located at this position (see Figure 6; also see Keel et al. 2014); (3) the high-velocity component has an $[\text{O III}]/\text{H}\beta$ emission-line flux ratio that is consistent with being dominated by AGN photoionization rather than a H II region

(see Harrison et al. 2014).

4.2.2. Quasar winds

A possible origin of the radio emission in radio-quiet quasars is accretion disk winds (see e.g., Shlosman et al. 1985; Murray et al. 1995; Proga et al. 2000; Crenshaw et al. 2003), which propagate through the surrounding interstellar medium (ISM) to produce non-thermal radio emission (Zakamska & Greene 2014; Nims et al. 2014). Based on the energy conserving outflow model of Faucher-Giguère & Quataert (2012), Nims et al. (2014) explored the observational signatures of these winds in the radio and X-rays. In their model, the wind causes a shock that propagates outwards into the ambient medium and can reach distances of $\gtrsim 1 \text{ kpc}$ with velocities $\sim 1000 \text{ km s}^{-1}$ (at this point it interacts with the ISM and decelerates). They predict a steep-spectral index of $\alpha \approx -1$, which is consistent with our observations (see Table 2). It is less clear what this model predicts for the morphology of the radio emission; however, the propagation of the wind is predicted to be influenced by the properties and distribution of the ISM, and it will preferentially escape along the path of “least resistance” (Faucher-Giguère & Quataert 2012) that could lead to a moderately collimated outflow. For the Teacup AGN, we find that the position of the ionized outflow, and the associated radio emission, is directed away from the dusty regions (Figure 6), which may be consistent with these predictions.

In the fiducial model of Nims et al. (2014), the interaction of the winds with the ISM is predicted to result in a radio luminosity of

$$\nu L_{\nu} \approx 10^{-5} \xi_{-2} L_{\text{AGN}} \left(\frac{L_{\text{kin}}}{0.05 L_{\text{AGN}}} \right), \quad (2)$$

where ξ_{-2} is the scaled efficiency (i.e., 1% of the shock energy goes into relativistic electrons), L_{AGN} is the bolometric luminosity of the AGN and L_{kin} is the kinetic luminosity of the wind. For the Teacup AGN, Nims et al. (2014) would predict a radio luminosity of $\nu L_{\nu} \approx 20 \times 10^{39} \text{ erg s}^{-1}$ (i.e., $L_{1.5\text{GHz}} \approx 13 \times 10^{23} \text{ W Hz}^{-1}$), using their fiducial values (i.e., $\xi_{-2} = 1$; $L_{\text{kin}} = 0.05 L_{\text{AGN}}$). This is a factor of ≈ 8 above the core radio luminosity, that we observe, of $\nu L_{\nu}(1.5 \text{ GHz}) = 2.6 \times 10^{39} \text{ erg s}^{-1}$ (i.e., $L_{1.5\text{GHz}} = 1.7 \times 10^{23} \text{ W Hz}^{-1}$). Given the nature of the simple model assumptions (e.g., the assumed properties of the ISM; see Nims et al. 2014), we can not use this discrepancy as strong evidence that the radio emission in the core of the Teacup AGN, and the associated outflow, are not driven by a quasar wind.

4.2.3. Compact jets and nuclear activity

Compact radio emission (i.e., on $\lesssim 5 \text{ kpc}$ scales) in radio-quiet quasars may be associated with nuclear coronal activity (i.e., the region around the AGN accretion disk) or compact radio jets (e.g., Kukula et al. 1998; Ulvestad et al. 2005; Leipski & Bennert 2006; Laor & Behar 2008). Nuclear coronal activity is predicted to produce flat spectral indices (i.e., $\alpha \approx 0$; Laor & Behar 2008), which is not what is observed in the Teacup AGN (Figure 2).

In contrast, the core emission in the Teacup AGN shares many characteristics with radio-loud (with

$L_{5\text{ GHz}} \gtrsim 10^{26} \text{ W Hz}^{-1}$) compact, steep spectrum quasars, that show steep radio spectra, have jets and lobes on small scales and exhibit broad [O III] emission-line profiles (e.g., Gelderman & Whittle 1994; see review in O’Dea 1998). In particular, it is plausible that the HR-B radio structure is a hot spot of a radio jet, where it interacts with the ionized gas in the local ISM and drives a high velocity outflow (see Figure 6). This is also analogous to previous observations of a small number of AGN showing compact jets interacting with the ionized gas (e.g., Capetti et al. 1999; Leipski & Bennert 2006; Barbosa et al. 2009; Stockton et al. 2007). We note that several radio-loud systems have also been observed to have high-velocity kinematic components of ionized gas, associated with radio jets, that are offset by several hundred km s^{-1} ; furthermore, in the most extreme cases the *line widths* for these radio-loud systems can be even greater than observed in the Teacup AGN (i.e., $\text{FWHM} \gtrsim 1000 \text{ km s}^{-1}$; e.g., Emonts et al. 2005; Holt et al. 2008; Nesvadba et al. 2008; Shih et al. 2013).

4.2.4. Summary of core region

Overall the radio emission and outflow in the core of the Teacup AGN are consistent with being produced by radio jets or quasar winds that are interacting with the ISM in the host galaxy. This interaction could result in the high-velocity ionized gas that we observe (see Figure 6 and Figure 7). The compact sizes and the narrow angular range of the radio emitting region in the core, in particular for the HR-B structure, may favor the jet scenario.

4.3. What produces the $\approx 10 \text{ kpc}$ bubbles?

The radio bubbles of the Teacup AGN (see Figure 6) are reminiscent of several of the large-scale ($\gtrsim 1\text{--}10 \text{ kpc}$) radio structures observed in local Seyferts (i.e., low luminosity AGN), that are often associated with optical emission-line regions and disturbed ionized gas (e.g., Capetti et al. 1996; Colbert et al. 1996; Falcke et al. 1998; Ferruit et al. 1999; Whittle & Wilson 2004; Hota & Saikia 2006; Kharb et al. 2006). Furthermore, the morphology of the large-scale arc of ionized gas in the Teacup AGN (Figure 6) is analogous to some local starburst galaxies and AGN that host “super bubbles”, or arcs/filaments of optical emission lines (e.g., Heckman et al. 1990; Veilleux et al. 1994, 2001, 2005; Capetti et al. 1996; Ferruit et al. 1999; Whittle & Wilson 2004; also see the analogous radio-loud AGN in van Breugel et al. 1985 and Hatch et al. 2013). These emission-line features are often attributed to the cooler edges of hot gas bubbles (with $\approx 10^{6\text{--}8} \text{ K}$) that are expanding and sweeping up the ambient ISM material (e.g., Heckman et al. 1990; Capetti et al. 1996; Greene et al. 2014). Simulations and theoretical models have shown that compact radio jets (i.e., $\lesssim 1 \text{ kpc}$), or quasar winds, can interact with an inhomogeneous ambient ISM, transfer energy and momentum and drive energy-conserving outflowing bubbles, which expand and accelerate more clouds on larger scales (e.g., Sutherland & Bicknell 2007; Faucher-Giguère & Quataert 2012; Zubovas & King 2012; Wagner et al. 2012, 2013). It is therefore possible that compact radio jets or a quasar wind, which may reside in the core regions (see Section 4.2), are responsible

for the $\approx 10\text{--}12 \text{ kpc}$ radio bubbles and the associated arc of ionized gas (Figure 1; Figure 3).

An analogous object to the Teacup AGN is the local Seyfert Mrk 6, which hosts 7.5 kpc radio bubbles and $\approx 1 \text{ kpc}$ radio jets. Kharb et al. (2006) suggests that the radio jets are ultimately responsible for the creation of the large-scale radio bubbles. Following Kharb et al. (2006), we can estimate the particle energy (electrons and protons; E_{min}) at minimum pressure in the radio bubbles, under the assumption of equipartition of energy between the magnetic field and relativistic electrons and neglecting thermal pressure. We calculate these values following equations (1) and (4) of O’Dea & Owen (1987) and obtain the relevant constants from Pacholczyk (1970); see Miley (1980) for a discussion on the relative assumptions. We assume spherical regions of radius $D/2$ (see Table 2) with a filling factor of $\phi = 1$, upper and lower frequency cut offs of $\nu_u = 10 \text{ GHz}$ and $\nu_l = 10 \text{ MHz}$, a spectral index of $\alpha = -0.9$ and use the 5.12 GHz flux densities (Table 2). The energy estimates also depend on the value k , which is the ratio of relativistic proton to relativistic electron energy. We consider a range of values of E_{min} by adopting the range $k = 1\text{--}4000$, which reflects the observed range found for the radio-filled X-ray cavities in clusters (Birzan et al. 2008). Using these assumptions, we find that the minimum particle energies are $E_{\text{min}} \approx (1.7\text{--}130) \times 10^{56} \text{ erg}$ and $E_{\text{min}} \approx (0.70\text{--}54) \times 10^{56} \text{ erg}$ for the eastern and western radio bubbles, respectively. We note that these estimates scale by $(\phi)^{3/7}$, such that if $\phi = 10^{-3}$ this would result in a factor of ≈ 20 decrease in the quoted values.

If we assume that the HR-A and HR-B structures are both dominated by radio jets with $\alpha = -1.1$ (see Table 2), their combined total radio luminosity is $2.5 \times 10^{40} \text{ erg s}^{-1}$ (following Equation (1) in O’Dea & Owen 1987) which would result in a jet kinetic luminosity of $2.5 \times 10^{42} \text{ erg s}^{-1}$, assuming that 1% of the total jet energy is converted into radio luminosity (following Kharb et al. 2006; also see e.g., Birzan et al. 2008). This would require the jets to deposit their energy continuously for $\approx 3.0\text{--}230 \text{ Myr}$ to produce the derived combined minimum energy of the bubbles. If the core radio luminosity is, instead, produced by a quasar wind with $L_{\text{kin}} = 1.3 \times 10^{43} \text{ erg s}^{-1}$, (following Equation 2; see Nims et al. 2014) the wind would need to deposit all of its energy over a timescale of $\approx 0.59\text{--}46 \text{ Myr}$. It is interesting to note that these are plausible timescales that are comparable to the typical ages, of $\approx 10\text{--}40 \text{ Myr}$, for the radio-filled X-ray cavities in local cooling clusters that have similar sizes to the radio bubbles of the Teacup AGN (Birzan et al. 2004). To further assess these ideas, spectral ageing techniques could be used on deeper radio observations of the bubbles that have a better sampled frequency range than performed here (e.g., see Harwood et al. 2013 and references there-in). Deep X-ray observations with *Chandra* will also enable us to measure the temperature and distribution of the hot gas around the Teacup AGN, establish if there is a hot gas component associated with the radio bubbles and measure, more reliably, the total energy content and lifetimes of the bubbles (following e.g., Birzan et al. 2004, 2008; Mingo et al. 2011; Greene et al. 2014).

5. CONCLUSIONS

We have presented VLA radio imaging, VIMOS/IFU optical spectroscopy and *HST* imaging on the Teacup AGN; a $z = 0.085$ type 2 radio-quiet quasar. Our main conclusions are as follows.

- The Teacup AGN hosts bi-polar radio bubbles extending $\approx 10\text{--}12$ kpc each side of the nucleus (see Section 3.1). The edge of the brighter, eastern bubble is spatially coincident with an arc of luminous ionized gas (see Section 3.2 and Section 3.3).
- High-resolution radio imaging of the central few kiloparsecs reveals that the core is dominated by two unresolved radio structures (at a resolution of $\text{HPBW} \approx 0.6$ kpc). These are a bright central structure and a fainter structure ≈ 0.8 kpc to the northeast (see Section 3.1). This fainter structure is co-spatial with a high-velocity ionized gas component ($v = -740 \text{ km s}^{-1}$; $v_{\text{max}} \approx 1100 \text{ km s}^{-1}$). This high-velocity kinematic component and corresponding radio structure are located at the base of the ≈ 12 kpc eastern bubble (see Section 4.1).
- We favor an interpretation where small-scale radio jets, or possibly quasar winds, are directly accelerating the gas on ≈ 1 kpc scales (see Section 4.2). The same jets or winds, are likely to be driving the large-scale radio bubbles that are interacting with the ISM on $\approx 10\text{--}12$ kpc scales (see Section 4.3).

The Teacup AGN exhibits many of the predicted features of a source that is the transition between an active phase of star formation and AGN activity to a quiescent elliptical galaxy via AGN feedback (following e.g., Hopkins et al. 2006), i.e., a post-merger galaxy that hosts an AGN that is injecting energy into the gas in the host galaxy. The *HST* imaging reveals that the Teacup AGN resides in a bulge-dominated galaxy, with shell-like features, indicative of previous merger activity (Figure 6; also see Keel et al. 2014). Additionally, the dust lanes in this galaxy also imply it was associated with a gas-rich merger (e.g., Shabala et al. 2012). This source is currently hosting quasar activity (Harrison et al. 2014) that

may be in decline (Gagne et al. 2014) and our new observations have revealed high-velocity ionized gas and radio bubbles that imply that considerable energy injection into the ISM is occurring on $\approx 1\text{--}12$ kpc scales, indicative of AGN feedback.

Our observations of the Teacup AGN shed some light on the observed correlation between radio luminosity and the ionized gas kinematics (i.e., outflow velocities) seen in radio-quiet AGN (Mullaney et al. 2013; Zakamska & Greene 2014). The radio emission in this radio-quiet AGN is tracing both a ≈ 1 kpc high-velocity outflow and $\approx 10\text{--}12$ kpc radio bubbles that are likely to both be AGN driven. In a future paper we will present high-resolution radio imaging of a larger sample of radio-quiet AGN that exhibit kiloparsec-scale ionized outflows to investigate the properties of their radio emission and to determine the role, or lack thereof, of radio jets in driving outflows and contributing to AGN feedback in these systems.

We thank the referee, William C. Keel, for his constructive comments. We acknowledge the Science and Technology Facilities Council (CMH and MTH through grant code ST/I505656/1; APT, DMA, ACE and AMS through grant code ST/I001573/1), and the Leverhulme Trust (DMA). FEB acknowledges support from CONICYT-Chile (Basal-CATA PFB-06/2007, FONDECYT 1141218, “EMBIGGEN” Anillo ACT1101), and Project IC120009 “Millennium Institute of Astrophysics (MAS)” funded by the Iniciativa Científica Milenio del Ministerio de Economía, Fomento y Turismo. JRM acknowledges support from the University of Sheffield via its Vice-Chancellor Fellowship scheme. The VLA is part of the National Radio Astronomy Observatory, which is a facility of the National Science Foundation operated under cooperative agreement by Associated Universities, Inc. Part of this work is based on observations made with the NASA/ESA *Hubble Space Telescope*, obtained from the Data Archive at the Space Telescope Science Institute, which is operated by the Association of Universities for Research in Astronomy, Inc., under NASA contract NAS 5-26555.

REFERENCES

- Alatalo, K., Blitz, L., Young, L. M., et al. 2011, *ApJ*, 735, 88
 Alexander, D. M., & Hickox, R. C. 2012, *NewAR*, 56, 93
 Alexander, D. M., Swinbank, A. M., Smail, I., McDermid, R., & Nesvadba, N. P. H. 2010, *MNRAS*, 402, 2211
 Arribas, S., Colina, L., Bellocchi, E., Maiolino, R., & Villar-Martín, M. 2014, *A&A*, 568, A14
 Barbosa, F. K. B., Storchi-Bergmann, T., Cid Fernandes, R., Winge, C., & Schmitt, H. 2009, *MNRAS*, 396, 2
 Becker, R. H., White, R. L., & Helfand, D. J. 1995, *ApJ*, 450, 559
 Bell, E. F. 2003, *ApJ*, 586, 794
 Benson, A. J., Bower, R. G., Frenk, C. S., et al. 2003, *ApJ*, 599, 38
 Birzan, L., McNamara, B. R., Nulsen, P. E. J., Carilli, C. L., & Wise, M. W. 2008, *ApJ*, 686, 859
 Birzan, L., Rafferty, D. A., McNamara, B. R., Wise, M. W., & Nulsen, P. E. J. 2004, *ApJ*, 607, 800
 Bower, R. G., Benson, A. J., Malbon, R., et al. 2006, *MNRAS*, 370, 645
 Brusa, M., Bongiorno, A., Cresci, G., et al. 2014, *arXiv:1409.1615*
 Capetti, A., Axon, D. J., Macchetto, F., Sparks, W. B., & Boksenberg, A. 1996, *ApJ*, 469, 554
 Capetti, A., Axon, D. J., Macchetto, F. D., Marconi, A., & Winge, C. 1999, *Mem. Soc. Astron. Italiana*, 70, 41
 Churazov, E., Sazonov, S., Sunyaev, R., et al. 2005, *MNRAS*, 363, L91
 Colbert, E. J. M., Baum, S. A., Gallimore, J. F., O’Dea, C. P., & Christensen, J. A. 1996, *ApJ*, 467, 551
 Condon, J. J., Kellermann, K. I., Kimball, A. E., Ivezić, Ž., & Perley, R. A. 2013, *ApJ*, 768, 37
 Crenshaw, D. M., Kraemer, S. B., & George, I. M. 2003, *ARA&A*, 41, 117
 Diamond-Stanic, A. M., Moustakas, J., Tremonti, C. A., et al. 2012, *ApJ*, 755, L26
 Emonts, B. H. C., Morganti, R., Tadhunter, C. N., et al. 2005, *MNRAS*, 362, 931
 Fabian, A. C. 2012, *ARA&A*, 50, 455
 Falcke, H., Wilson, A. S., & Simpson, C. 1998, *ApJ*, 502, 199
 Faucher-Giguère, C.-A., & Quataert, E. 2012, *MNRAS*, 425, 605
 Ferruit, P., Wilson, A. S., Falcke, H., et al. 1999, *MNRAS*, 309, 1
 Feruglio, C., Maiolino, R., Piconcelli, E., et al. 2010, *A&A*, 518, L155

- Gagne, J. P., Crenshaw, D. M., Kraemer, S. B., et al. 2014, *ApJ*, 792, 72
- Gaspari, M., Melioli, C., Brighenti, F., & D’Ercole, A. 2011, *MNRAS*, 411, 349
- Gelderman, R., & Whittle, M. 1994, *ApJS*, 91, 491
- Genzel, R., Newman, S., Jones, T., et al. 2011, *ApJ*, 733, 101
- Genzel, R., Förster Schreiber, N. M., Rosario, D., et al. 2014, *arXiv:1406.0183*
- Greene, J. E., Pooley, D., Zakamska, N. L., Comerford, J. M., & Sun, A.-L. 2014, *ApJ*, 788, 54
- Greene, J. E., Zakamska, N. L., Ho, L. C., & Barth, A. J. 2011, *ApJ*, 732, 9
- Guillard, P., Ogle, P. M., Emonts, B. H. C., et al. 2012, *ApJ*, 747, 95
- Harrison, C. M., Alexander, D. M., Mullaney, J. R., & Swinbank, A. M. 2014, *MNRAS*, 441, 3306
- Harrison, C. M., Alexander, D. M., Swinbank, A. M., et al. 2012, *MNRAS*, 426, 1073
- Harwood, J. J., Hardcastle, M. J., Croston, J. H., & Goodger, J. L. 2013, *MNRAS*, 435, 3353
- Hatch, N. A., Röttgering, H. J. A., Miley, G. K., et al. 2013, *MNRAS*, 436, 2244
- Heckman, T. M., Armus, L., & Miley, G. K. 1990, *ApJS*, 74, 833
- Heckman, T. M., & Best, P. N. 2014, *ARA&A*, 52, 589
- Heckman, T. M., Miley, G. K., van Breugel, W. J. M., & Butcher, H. R. 1981, *ApJ*, 247, 403
- Heckman, T. M., Borthakur, S., Overzier, R., et al. 2011, *ApJ*, 730, 5
- Helou, G., Soifer, B. T., & Rowan-Robinson, M. 1985, *ApJ*, 298, L7
- Holt, J., Tadhunter, C. N., & Morganti, R. 2008, *MNRAS*, 387, 639
- Hopkins, P. F., Hernquist, L., Cox, T. J., et al. 2006, *ApJS*, 163, 1
- Hota, A., & Saikia, D. J. 2006, *MNRAS*, 371, 945
- Husemann, B., Wisotzki, L., Sánchez, S. F., & Jahnke, K. 2013, *A&A*, 549, A43
- Ivion, R. J., Magnelli, B., Ibar, E., et al. 2010, *A&A*, 518, L31
- Keel, W. C., Chojnowski, S. D., Bennert, V. N., et al. 2012, *MNRAS*, 420, 878
- Keel, W. C., Maksym, W. P., Bennert, V. N., et al. 2014, *arXiv:1408.5159*
- Kellermann, K. I., Sramek, R., Schmidt, M., Shaffer, D. B., & Green, R. 1989, *AJ*, 98, 1195
- Kennicutt, Jr., R. C. 1998, *ARA&A*, 36, 189
- Kharb, P., O’Dea, C. P., Baum, S. A., Colbert, E. J. M., & Xu, C. 2006, *ApJ*, 652, 177
- Kim, M., Ho, L. C., Lonsdale, C. J., et al. 2013, *ApJ*, 768, L9
- Kimball, A. E., Kellermann, K. I., Condon, J. J., Ivezić, Ž., & Perley, R. A. 2011, *ApJ*, 739, L29
- Kormendy, J., & Ho, L. C. 2013, *ARA&A*, 51, 511
- Kukula, M. J., Dunlop, J. S., Hughes, D. H., & Rawlings, S. 1998, *MNRAS*, 297, 366
- Lal, D. V., & Ho, L. C. 2010, *AJ*, 139, 1089
- Laor, A., & Behar, E. 2008, *MNRAS*, 390, 847
- Le Fèvre, O., Saisse, M., Mancini, D., et al. 2003, in *Society of Photo-Optical Instrumentation Engineers (SPIE) Conference Series*, Vol. 4841, *Instrument Design and Performance for Optical/Infrared Ground-based Telescopes*, ed. M. Iye & A. F. M. Moorwood, 1670–1681
- Lehnert, M. D., Tasse, C., Nesvadba, N. P. H., Best, P. N., & van Driel, W. 2011, *A&A*, 532, L3
- Leipski, C., & Bennert, N. 2006, *A&A*, 448, 165
- Leipski, C., Falcke, H., Bennert, N., & Hüttemeister, S. 2006, *A&A*, 455, 161
- Lintott, C. J., Schawinski, K., Slosar, A., et al. 2008, *MNRAS*, 389, 1179
- Liu, G., Zakamska, N. L., Greene, J. E., Nesvadba, N. P. H., & Liu, X. 2013, *MNRAS*, 436, 2576
- Mahony, E. K., Morganti, R., Emonts, B. H. C., Oosterloo, T. A., & Tadhunter, C. 2013, *MNRAS*, 435, L58
- McCarthy, I. G., Schaye, J., Ponman, T. J., et al. 2010, *MNRAS*, 406, 822
- McNamara, B. R., & Nulsen, P. E. J. 2012, *New Journal of Physics*, 14, 055023
- Miley, G. 1980, *ARA&A*, 18, 165
- Mingo, B., Hardcastle, M. J., Croston, J. H., et al. 2011, *ApJ*, 731, 21
- Morganti, R., Frieswijk, W., Oonk, R. J. B., Oosterloo, T., & Tadhunter, C. 2013, *A&A*, 552, L4
- Morganti, R., Oosterloo, T. A., Tadhunter, C. N., van Moorsel, G., & Emonts, B. 2005, *A&A*, 439, 521
- Mullaney, J. R., Alexander, D. M., Fine, S., et al. 2013, *MNRAS*, 433, 622
- Murphy, E. J., Stierwalt, S., Armus, L., Condon, J. J., & Evans, A. S. 2013, *ApJ*, 768, 2
- Murray, N., Chiang, J., Grossman, S. A., & Voit, G. M. 1995, *ApJ*, 451, 498
- Nelson, C. H., & Whittle, M. 1996, *ApJ*, 465, 96
- Nesvadba, N. P. H., Lehnert, M. D., De Breuck, C., Gilbert, A. M., & van Breugel, W. 2008, *A&A*, 491, 407
- Nesvadba, N. P. H., Lehnert, M. D., Eisenhauer, F., et al. 2006, *ApJ*, 650, 693
- Nesvadba, N. P. H., Polletta, M., Lehnert, M. D., et al. 2011, *MNRAS*, 415, 2359
- Nims, J., Quataert, E., & Faucher-Giguere, C.-A. 2014, *arXiv:1408.5141*
- O’Dea, C. P. 1998, *PASP*, 110, 493
- O’Dea, C. P., & Owen, F. N. 1987, *ApJ*, 316, 95
- Oosterloo, T. A., Morganti, R., Tzioumis, A., et al. 2000, *AJ*, 119, 2085
- Osterbrock, D. E. 1989, *Astrophysics of gaseous nebulae and active galactic nuclei*, ed. Osterbrock, D. E.
- Pacholczyk, A. G. 1970, *Radio astrophysics. Nonthermal processes in galactic and extragalactic sources*
- Proga, D., Stone, J. M., & Kallman, T. R. 2000, *ApJ*, 543, 686
- Reyes, R., Zakamska, N. L., Strauss, M. A., et al. 2008, *AJ*, 136, 2373
- Rupke, D. S., Veilleux, S., & Sanders, D. B. 2005a, *ApJS*, 160, 87
- , 2005b, *ApJS*, 160, 115
- Rupke, D. S. N., & Veilleux, S. 2013, *ApJ*, 768, 75
- Schaye, J., Crain, R. A., Bower, R. G., et al. 2014, *arXiv:1407.7040*
- Sell, P. H., Tremonti, C. A., Hickox, R. C., et al. 2014, *MNRAS*, 441, 3417
- Shabala, S. S., Ting, Y.-S., Kaviraj, S., et al. 2012, *MNRAS*, 423, 59
- Shih, H.-Y., Stockton, A., & Kewley, L. 2013, *ApJ*, 772, 138
- Shlosman, I., Vitello, P. A., & Shaviv, G. 1985, *ApJ*, 294, 96
- Silk, J., & Rees, M. J. 1998, *A&A*, 331, L1
- Singh, V., Ishwara-Chandra, C. H., Wadadekar, Y., Beelen, A., & Kharb, P. 2014, *arXiv:1410.2720*
- Solórzano-Iñarrea, C., & Tadhunter, C. N. 2003, *MNRAS*, 340, 705
- Sopp, H. M., & Alexander, P. 1991, *MNRAS*, 251, 14P
- Stockton, A., Canalizo, G., Fu, H., & Keel, W. 2007, *ApJ*, 659, 195
- Sutherland, R. S., & Bicknell, G. V. 2007, *ApJS*, 173, 37
- Ulvestad, J. S., Antonucci, R. R. J., & Barvainis, R. 2005, *ApJ*, 621, 123
- van Breugel, W., Miley, G., Heckman, T., Butcher, H., & Bridle, A. 1985, *ApJ*, 290, 496
- Veilleux, S. 1991, *ApJS*, 75, 383
- Veilleux, S., Cecil, G., & Bland-Hawthorn, J. 2005, *ARA&A*, 43, 769
- Veilleux, S., Cecil, G., Bland-Hawthorn, J., et al. 1994, *ApJ*, 433, 48
- Veilleux, S., Shopbell, P. L., & Miller, S. T. 2001, *AJ*, 121, 198
- Veilleux, S., Meléndez, M., Sturm, E., et al. 2013, *ApJ*, 776, 27
- Villar Martín, M., Emonts, B., Humphrey, A., Cabrera Lavers, A., & Binette, L. 2014, *MNRAS*, 440, 3202
- Villar-Martín, M., Tadhunter, C., Morganti, R., Axon, D., & Koekemoer, A. 1999, *MNRAS*, 307, 24
- Vogelsberger, M., Genel, S., Springel, V., et al. 2014, *MNRAS*, 444, 1518
- Wagner, A. Y., Bicknell, G. V., & Umemura, M. 2012, *ApJ*, 757, 136
- Wagner, A. Y., Umemura, M., & Bicknell, G. V. 2013, *ApJ*, 763, L18
- Wampler, E. J., Burbidge, E. M., Baldwin, J. A., & Robinson, L. B. 1975, *ApJ*, 198, L49
- Whittle, M. 1992, *ApJ*, 387, 109
- Whittle, M., & Wilson, A. S. 2004, *AJ*, 127, 606
- Wilson, A. S., & Heckman, T. M. 1985, in *Astrophysics of Active Galaxies and Quasi-Stellar Objects*, ed. J. S. Miller, 39–109

Xu, C., Livio, M., & Baum, S. 1999, *AJ*, 118, 1169
Zakamska, N. L., & Greene, J. E. 2014, *MNRAS*, 442, 784

Zakamska, N. L., Strauss, M. A., Heckman, T. M., Ivezić, Ž., &
Krolik, J. H. 2004, *AJ*, 128, 1002
Zubovas, K., & King, A. 2012, *ApJ*, 745, L34